

Time-domain effects of rigid sphere scattering on measurement of transient plane waves

Michael B. Muhlestein,^{a)} Derek C. Thomas, and Kent L. Gee

Department of Physics and Astronomy, N-283 Eyring Science Center, Brigham Young University, Provo, Utah 84602

(Received 12 October 2013; revised 14 May 2014; accepted 27 May 2014)

Transient waves, like all other acoustic waves, will diffract around solid objects, such as measurement instrumentation. A derivation of an impulse response function on the surface of a rigid sphere, based on linear, classical scattering theory, is presented. The theoretical impulse response function is validated using an experiment with blast noise. An application of the impulse response function to a rocket noise measurement is discussed. The impulse response function shows that the presence of the rigid sphere significantly affects the measurement and estimation of rocket-noise waveforms, power spectral densities, and statistical measures. © 2014 Acoustical Society of America.

[\[http://dx.doi.org/10.1121/1.4883381\]](http://dx.doi.org/10.1121/1.4883381)

PACS number(s): 43.20.Px [RR]

Pages: 13–21

I. INTRODUCTION

One method to characterize complicated sources, such as the supersonic jets associated with solid rocket motors and military aircraft, is to map the acoustic intensity surrounding the source.¹ Instruments that estimate intensity, or intensity probes, by acoustical measurement must necessarily be placed in the sound field and will therefore generate a scattered field which will affect measurements of the field. While there is a large body of published research concerning the diffraction of time-harmonic signals by instrumentation,^{2,3} there is significantly less published concerning the diffraction of transient signals, such as acoustic shocks. This paper contains an analysis of the measurement of transient plane waves by an intensity probe consisting of a tetrahedral array of microphones embedded in a rigid sphere. This probe was chosen because of its simple geometry and the easily calculable diffraction of sound about it.⁴

The diffraction of sound pulses was studied as early as 1901 by Sommerfeld⁵ and 1910 by Lamb.⁶ Lamb used a Fourier analysis technique to study the diffraction of pulses by a semi-infinite plane but could only obtain a closed form for incident pulses with known Fourier transforms. Mitzner⁷ was able to use numerical methods to find the scattered field of an arbitrary transient wave by an arbitrarily shaped hard surface using a retarded potential technique, and presented the case of a Gaussian pulse incident upon a rigid sphere as an example. Soules and Mitzner calculated the diffraction of a pulse by a rigid sphere using numerical Fourier transformation in 1966, but since the study is unpublished, the details are unknown. All of these studies have been confined to smooth pulses, and they do not explicitly consider the pressure on a rigid sphere due to arbitrary waves, specifically waves containing rapid transients such as those present in acoustic shock waves. On the other hand, Tanno *et al.*,⁸

experimentally found the pressure on the surface of a rigid sphere due to an incident shock wave using a shock tube. Feuillade⁹ used numerical Fourier transformations to calculate the impulse response from rigid, pressure release, and movable fluid spheres to create educational animations of scattering from spheres, but he limited the calculation of the impulse response to a far-field measurement location.

The purpose of this paper is to present a method by which diffraction effects on the measurement of acoustic waves with shock-like features on the surface of a rigid sphere may be quantitatively described. The term “shock-like” is used because the mathematical treatment of the scattering will be purely linear. A secondary purpose of this study is to help develop intuition about the time-domain effects of the scattering of shocks due to instrumentation. First, classical linear scattering theory is used to develop an impulse response function for the measurement of progressive plane waves by a sphere. While the approach used in this paper—using numerical inverse Fourier transformation on several harmonic solutions to the rigid-sphere problem—is not new, the advances in computational power since Lamb’s work enable this approach to be a viable option. The validity of the impulse response function is shown by comparing blast noise measured by a stand-alone microphone with blast noise measured by a spherical intensity probe. Finally, an analysis of a measurement of noise radiating from a GEM-60 solid rocket motor by a spherical intensity probe is presented. The effects of the presence of the probe on the estimation of the pressure waveforms, spectra, and time-domain statistics are discussed.

II. DEVELOPMENT OF THE IMPULSE RESPONSE FUNCTION ON THE SURFACE OF A RIGID SPHERE

A. Theory

The probe studied for this paper has been described by Gee *et al.*,^{1,10} and it is shown in Fig. 1. The probe has a spherical aluminum casing, a diameter of 2.54 cm, and four 1/4 in. (6.35 mm) G.R.A.S. 40BH microphones embedded in

^{a)}Author to whom correspondence should be addressed. Electronic mail: mimuhle@utexas.edu

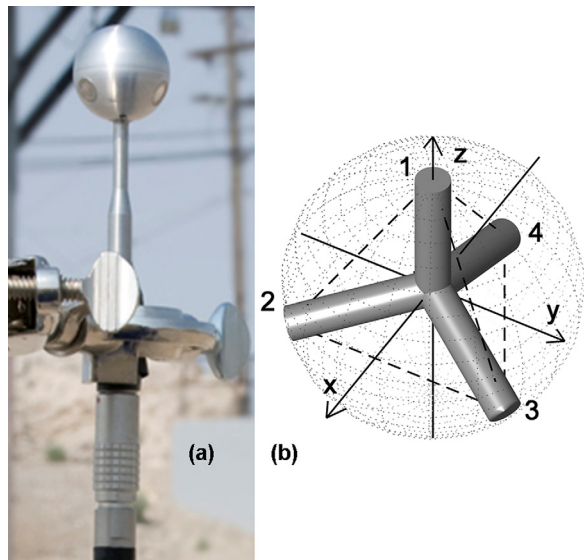


FIG. 1. (Color online) (a) A picture of the spherical probe used in this paper. (b) A schematic of the tetrahedral array of microphone positions used in the probe.

it such that the diaphragms are flush with the aluminum casing (no grid caps are used). A thin, hollow, aluminum stem (diameter of 4 mm) for the wiring of the electronics inside the probe is attached to the probe. The mounting point of the stem is referred to as the bottom of the sphere. A microphone is located on the top and, along with the other three microphones, forms a tetrahedral array. We model the probe as a uniform, stationary, rigid sphere. The rigid-sphere model neglects the effects of radiation pressure on the microphone diaphragms, the presence of the wiring stem, the finite impedances of the aluminum casing and the microphones, and the fact that the microphone diaphragms are flat surfaces embedded in a sphere, as well as any geometrical deviations from a perfect sphere. We assume that all incident waves are planar. This is a reasonable assumption if the sound source is far from the probe.

Acoustic shock propagation is inherently nonlinear, so the choice to analyze the scattering of shocks using linear theory should be justified. The effects of the nonlinearity can be separated into cumulative effects and local effects.¹¹ Cumulative nonlinear effects increase with propagation distance and are usually characterized by some nonlinear distortion length, such as the shock formation distance of an initially sinusoidal signal propagating without losses.¹¹ Since we are interested only in the scattering of a wave in the space close to the instrumentation and because the probe dimensions are much smaller than the shock formation distance of initially sinusoidal waves with similar amplitudes and characteristic frequencies as the waves considered, cumulative nonlinear effects will be neglected for this study. Local nonlinear effects do not vary based on propagation distance. An example of a phenomenon involving local nonlinear distortion is the reflection of high-amplitude sound waves from a rigid surface. Local nonlinear effects only become significant with amplitudes much higher than those considered in this paper (the pressure due to a 160 dB re

20 μ Pa plane wave normally incident on a flat surface differs from the linear theory by less than 1%),¹² and so these effects will be neglected as well. It is possible that the local nonlinearities associated with scattering of shocks from curved surfaces (such as a rigid sphere or a long berm¹³) are not negligible, but these will not be considered for the present study. Therefore, all analyses presented here are based on linear approximations.

The diffraction of time-harmonic plane waves by a rigid sphere has been studied extensively.^{14–16} The solution for the total field at any distance $r \geq a$ from the sphere, where a is the radius of the sphere, is given by

$$\hat{p}_T = \hat{p}_I + \hat{p}_S = \hat{A}e^{-ikr\cos(\theta)} - \hat{A} \sum_{n=1}^{\infty} (2n+1) i^n \frac{j'_n(ka)}{h_n^{(2)'}(ka)} h_n^{(2)}(kr) P_n(\cos(\theta)) \quad (1)$$

where \hat{p}_T is the total complex pressure field, $\hat{p}_I = \hat{A} \exp(-ikr\cos(\theta))$ is the incident complex pressure field, \hat{p}_S is the complex scattered pressure field, \hat{A} is the complex amplitude of the incident field, k is the wave number, θ is the polar angle such that $\theta = 0$ is the direction the incident wave propagates from (see Fig. 2 for geometry), $j_n(x)$ is the n th order, spherical Bessel function of the first kind, $h_n^{(2)}(x)$ is the n th order, spherical Hankel function of the second kind [that is, $h_n^{(2)}(x) = j_n(x) - iy_n(x)$, where $y_n(x)$ is the n th order, spherical Neumann function], the primes denote differentiation with respect to the argument of the function, and $P_n(x)$ are the Legendre polynomials. The incident time-harmonic plane wave propagating in the positive z direction is described as $e^{i\omega t - ikz}$.

The plots in Fig. 3 show the magnitude of the n th term of \hat{p}_S relative to the largest term in the \hat{p}_S series for angles $\theta = 0^\circ$ and 90° , and for values of $ka = 0.1, 1,$ and 25 . The maximum value of ka used for the experiments below is 23.8 based on a sampling rate of 204 800 samples/s, so ensuring that the series converges for $ka = 25$ is sufficient

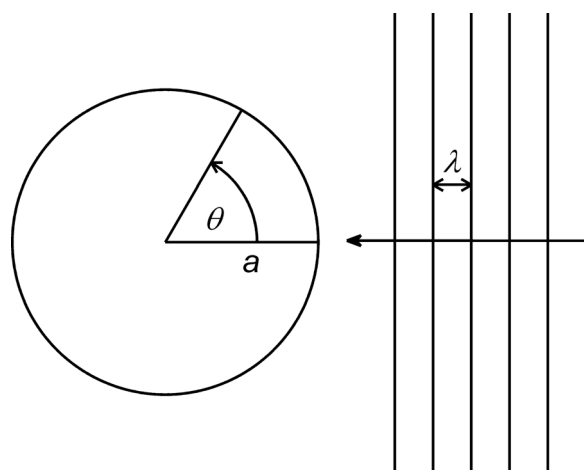


FIG. 2. Schematic of the orientation of a spherical probe relative to an incoming plane wave with wavelength λ . The sphere has a radius of a , and the angle on the surface of the sphere relative to the angle of normal incidence is θ .

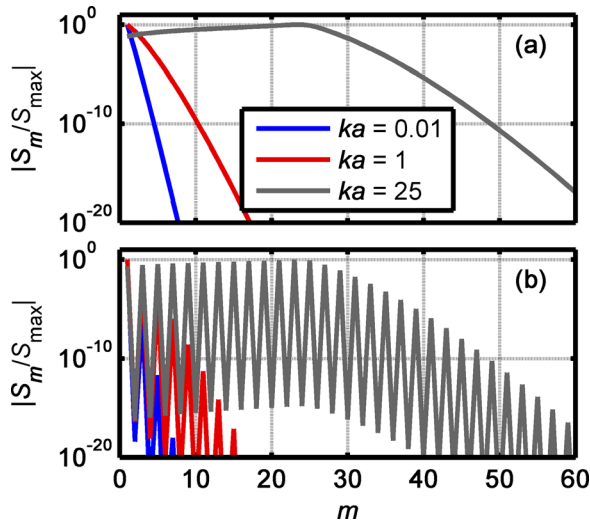


FIG. 3. (Color online) Convergence of the scattering pressure series. The curves in (a) are the absolute value of the m th term in the scattering series (S_m) divided by the maximum term in the series (S_{\max}), evaluated at $\theta = 0^\circ$ and for three values of ka . The curves in (b) are the same as in (a), but evaluated at $\theta = 90^\circ$.

for the purposes of this paper. If we require that all terms greater than 10^{-10} times the largest term in the series are included, then the results presented in Fig. 3 suggest that the inclusion of 50 terms in the series yields sufficient precision.

We refer to the ratio of the total pressure on the surface of the sphere to the incident pressure as the angle-dependent frequency response function, $H(f, \theta)$. The frequency response function predicts what phase and amplitude will be measured on the surface of a rigid sphere of radius a at a given angle θ due to an incident sinusoidal wave with frequency $f = c/\lambda$. It is more convenient to analyze the frequency response function in terms of the dimensionless quantity $ka = 2\pi fa/c$, rather than the frequency directly. Therefore, the frequency response function $H(ka, \theta)$ has been plotted in Fig. 4 for five angles of interest—normal incidence, or the front of the sphere (0°), grazing incidence (90°), the back of the sphere (180°), and the two intermediate angles (45° and 135°). As can be seen in Fig. 4, low frequency (ka) measurements ($ka < 0.2$) are not significantly

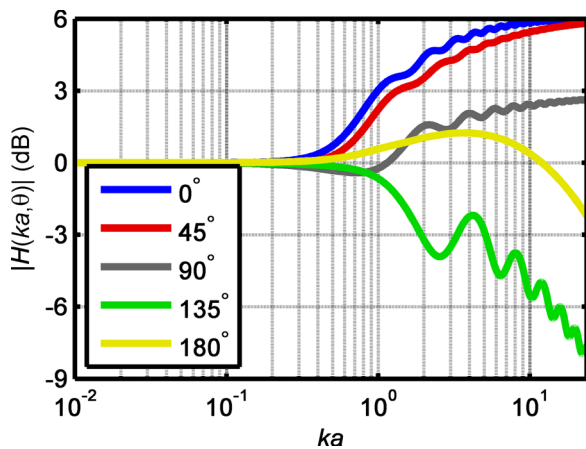


FIG. 4. (Color online) Frequency response function on a rigid sphere [FRF, or $H(k, \theta)$] as a function of ka , and evaluated at the five angles listed in the legend on the sphere relative to the incident sound field.

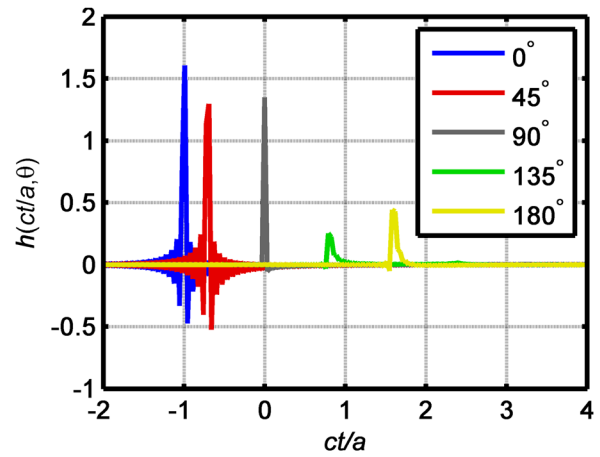


FIG. 5. (Color online) Impulse response function on the surface of a rigid sphere [IRF, or $h(ct/a, \theta)$]. Given an incident pressure wave in the form of a unit delta function, the IRF $h(ct/a, \theta)$ is what would be measured on the sphere at angle θ .

affected by the presence of the sphere while higher frequency measurements ($ka > 0.5$) are significantly affected by the presence of the sphere.

Performing an inverse Fourier transform on $H(f, \theta)$ with respect to f produces an impulse response function for measurements on the sphere, $h(t, \theta)$. The impulse response function (IRF) on the surface of a sphere can be studied as a function of the nondimensional time ct/a . Figure 5 shows $h(ct/a, \theta)$ evaluated for several angles of interest. The IRF was produced with 2^{20} frequencies, ranging from $\pm 409\,600$ Hz, and a sphere of radius 1.27 cm. The IRFs consist of a large peak and, for angles less than 90° , surrounding oscillations, which are due to the leakage associated with using a finite number of frequencies. The time associated with the peak of $h(ct/a, \theta)$ indicates the time at which a wavefront would arrive at the surface of the sphere relative to the time the same wavefront would arrive at the origin (center of the sphere) if the sphere were not present. For example, since the location of the 0° measurement is a distance a from the origin in a direction parallel to the direction of propagation, the peak of $h(ct/a, 0^\circ)$ would be expected to be at -1 , which is the case in Fig. 5. Similarly, since the location of the 90° measurement is in the direction perpendicular to the direction of propagation relative to the origin, the expected value of ct/a would be 0, which is the case in Fig. 5 as well. However, the time of arrival associated with the location at 180° on the sphere surface is not at 1, since all acoustic energy that reaches that location must be diffracted around the sphere, increasing the propagation distance. For very small angles, the expected pressure response is significantly higher than unity due to the wave reflected from the sphere. Note that without the sphere, the pressure response would be one. The response continues to decrease with increasing angle until the angle approaches 180° , which corresponds the back of the sphere, as can be seen in Fig. 5.

There are two ways that the results from this rigid-sphere model are used to analyze measured time-domain data. First, estimates of the incident waveform can be made by removing the effects of scattering from measurements of the pressure on the surface of the sphere. Second, an incident

pressure waveform can be convolved with the IRF to estimate what the pressure on the surface of a sphere would be. In both cases, it is important to remember the assumptions used to obtain the IRF. The incident field should be approximately planar near a sensor with spherical geometry, and the amplitudes must be low enough that local and cumulative nonlinear effects can be neglected in the neighborhood of the sphere. The direction of the incident field must also be known so that an appropriate coordinate system can be chosen. The actual convolution and deconvolution calculations have been carried out using Fourier transforms of the IRF and the pressure data.

Methods for convolution are well known; the method that is implemented in this paper consists of multiplying the Fourier transform of the IRF for the location of interest on the surface of the rigid sphere and the Fourier transform of the incident pressure waveform together, and then performing an inverse Fourier transform on the product. Removing the effects of scattering consists of a deconvolution, performed directly or by using the Fourier transform.

B. Validation of theory

Blast noise was used to validate the impulse response function (IRF) described in Sec. II A. Balloons filled with acetylene and oxygen can be used as consistent and relatively safe sources of blast noise,¹⁷ and they were used as the blast noise source of the validation experiment. The experiment was conducted in conjunction with another, as yet unpublished, study performed on the Bonneville Salt Flats. The Bonneville Salt Flats is a salt pan located in western Utah, and it is considered an approximate infinite rigid plane for the purposes of this study. A 43 cm diameter balloon, filled with a mixture of 0.42 mol of acetylene and 1.05 mol of oxygen was attached to the top of an extendable tripod, raised to a height of 4 m above the ground, and ignited. The spherical probe was placed 30.5 m (100 ft) from the balloon ignition location, and raised 1.5 m above the ground. The probe was oriented using the geometry in Fig. 1(b) such that Mic. 1 was vertical and the measurement angles were $\theta = 90^\circ, 57^\circ, 57^\circ,$ and 161° , with some possible uncertainty ($< 5^\circ$) due to alignment error in the field. A reference microphone, approximately 4 m away from the spherical probe but with the same radius to the explosion site, also measured the blast noise. The measurements were made in somewhat gusty wind conditions with a light breeze between gusts of wind. In order to minimize the presence of wind noise, measurements were made between the gusts of wind. The acoustic data were acquired at 204 800 samples/s ($4.9 \mu\text{s}/\text{sample}$) using a National Instruments (Austin, TX) PXI-based system using 24-bit PXI-4462 cards controlled by labview-based (National Instruments, Austin, TX) software. Post-processing of the data was performed using MATLAB.

The waveform recorded by the reference microphone is shown in Fig. 6(a), and a more detailed plot of the leading shock waveform, normalized by the peak amplitude of the leading shock p_0 , is shown in Fig. 6(b). Both the leading shock (which arrives at 0 ms) and a secondary, reflected shock (the reflection from the ground, which arrives at

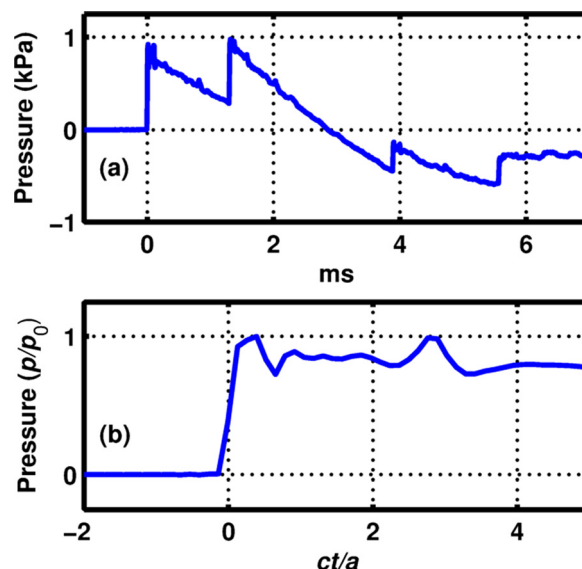


FIG. 6. (Color online) (a) A blast wave of an exploding acetylene and oxygen balloon measured by a reference microphone. The amplitude of the waveform in (b) has been normalized by the peak measured shock amplitude.

1.3 ms) are clearly evident in the waveform shown in Fig. 6(a).

Portions of the blast waveforms measured by the spherical probe microphone are shown in Fig. 7(a), and a more

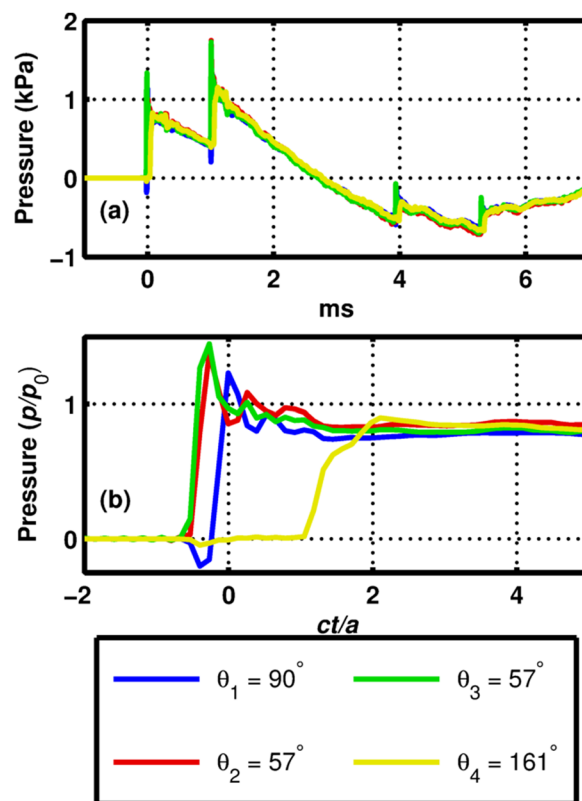


FIG. 7. (Color online) Measured blast wave of an exploding acetylene and oxygen balloon. The waveforms were recorded by an array of four microphones embedded in a spherical probe of radius 1.27 cm. The amplitudes of the waveforms in (b) have been normalized by the peak shock amplitude of the reference microphone, and the time array has been normalized by the probe radius and the sound speed.

TABLE I. A summary of various metrics used to describe the leading shock wave radiating from an exploding balloon. The waveforms used were measured by four microphones embedded in a 2.54 mm diameter, aluminum sphere. The metrics for the waveforms that have the effects of rigid-sphere scattering numerically removed are given in parentheses.

Probe Array ($a = 2.5$ cm)	Angle ($^\circ$)	Arrival time (μ s)	δ_L	Rise time (μ s)
Mic. 1	90	0 (0)	0.0107 (0.0098)	14.6 (9.8)
Mic. 2	57	-90 (4.9)	0.0119 (0.0073)	14.6 (4.9)
Mic. 3	57	-100 (4.9)	0.0125 (0.0083)	14.6 (9.8)
Mic. 4	161	54 (0)	0.0077 (0.0082)	39.1 (9.8)
Reference Mic.			0.0087	19.5

detailed plot of the leading shock waveform, normalized by the peak amplitude of the leading shock p_0 measured by the reference microphone, is shown in Fig. 7(b). The angle dependent effects of scattering are clearly apparent in the waveforms. The microphones positioned closer to the balloon show significantly higher peak shock amplitudes than the microphones positioned farther from the balloon. In addition, the arrival times of the shocks change depending on where the microphone is located.

Estimates of the leading and secondary shock arrival time, leading and secondary shock strength, and leading and secondary shock rise times from each of the probe microphones and the reference microphone (for comparison) are given in Table I and Table II. The arrival times for each shock are adjusted such that the leading shock measured by the top microphone arrives at 0 ms. The shock strength is a non-dimensional parameter used to characterize the amplitude of a shock, and is defined by Temkin¹⁸ as

$$\delta = \frac{(p_2 - p_1)}{p_1 + p_{\text{atm}}}, \quad (2)$$

where p_2 is the peak shock pressure, p_1 is the pressure just before the shock, and p_{atm} is the atmospheric pressure. Since there are two large shocks present in the waveforms, the leading shock strength will be denoted δ_L and the secondary, reflected shock strength will be denoted δ_S . The rise time of a shock is the difference between the time of arrival of the peak of a shock and the time of arrival of the base of the shock. Shock arrival and rise times are restricted to integer

TABLE II. A summary of various metrics used to describe the secondary shock wave radiating from an exploding balloon. The waveforms used were measured by four microphones embedded in a 2.54 mm diameter, aluminum sphere. The metrics for the waveforms that have the effects of rigid-sphere scattering numerically removed are given in parentheses. The arrival time is relative to the arrival time of the leading shock.

Probe Array ($a = 2.5$ cm)	Angle ($^\circ$)	Relative arrival time (ms)	δ_S	Rise time (μ s)
Mic. 1	90	1.02 (1.0)	0.0085 (0.0071)	29.3 (19.5)
Mic. 2	57	1.03 (1.0)	0.0122 (0.0075)	9.8 (9.8)
Mic. 3	57	1.02 (1.0)	0.0123 (0.0081)	14.6 (9.8)
Mic. 4	161	0.96 (1.0)	0.0068 (0.0090)	112 (9.8)
Reference Mic.		1.3	0.0066	24.4

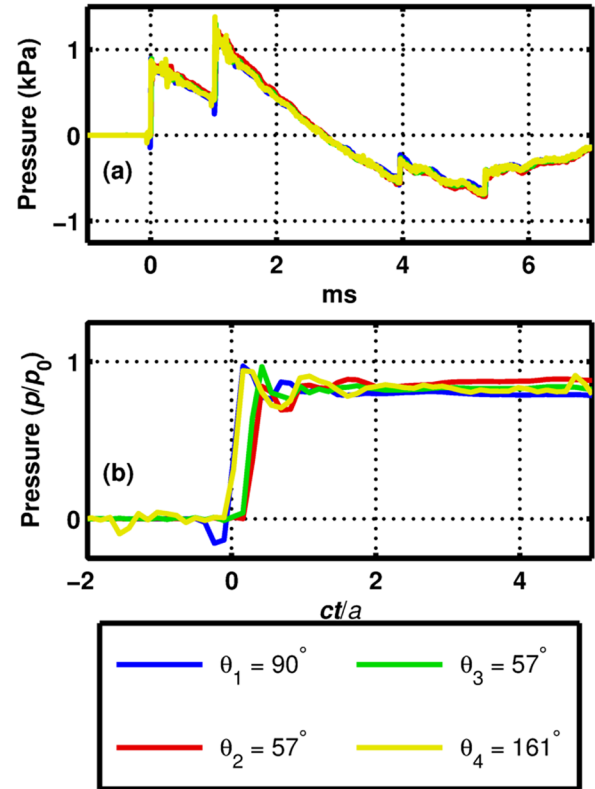


FIG. 8. (Color online) Estimated incident waveforms found by deconvolving the impulse response function of a rigid sphere from the waveforms measured by the spherical probe (shown in Fig. 6). The amplitudes of the waveforms in (b) have been normalized by the peak shock amplitude of microphone 1 from the reference array, and the time array has been normalized by the probe radius and the sound speed.

multiples of 4.9μ s, due to the temporal resolution of the experiment.

Estimates of the incident blast can be found from each of the four microphones by numerically deconvolving the IRF of the rigid sphere from the waveforms measured by the probe, thus estimates of the incident blast can be calculated for each of the four microphones. Since the reflected shock wave arrives significantly after the direct wave relative to the noticeable duration of the impulse response function (the impulse response functions in Fig. 4 appear to fall off to nearly 0 by about $ct/a = 5$ and the reflected shock arrives at $ct/a > 100$), the presence of the reflected shock will not alter the deconvolution in any significant manner. The estimates of the incident waveform are shown in Fig. 8(a), a more detailed plot of the leading shocks are shown, normalized by the reference microphone peak amplitude, in Fig. 8(b), and the quantitative metrics describing the shocks are given in Table I and Table II as the quantities in parentheses. While the deconvolved waveforms are not identical to each other, they are more similar to each other than the original waveforms in Fig. 7. Comparing the metrics associated with the original waveforms and the numerically deconvolved waveforms shows that all of the measures are much more uniform after the numerical deconvolution. For example, the estimates of δ_L and δ_S from the measured waveforms are 23%, 37%, 43%, and -11% for Microphones 1-4, respectively, greater than the reference estimates of δ_L and δ_S . Whereas

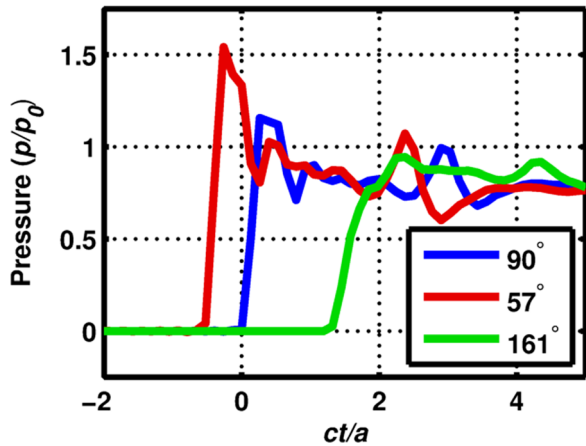


FIG. 9. (Color online) A model of a blast wave radiating from an exploding balloon and the predicted response of microphones embedded in a spherical probe at three angles. The amplitudes have been set such that the peak shock amplitude of the incident wave is unity.

the estimates for δ_L and δ_S for the deconvolved waveforms measured at Microphones 1–4 are only -13% , 16% , 4.6% , and 5.7% , respectively, greater than the reference shock strength estimate. The uniformity of the waveforms and metrics for the deconvolved waveforms suggests that the IRF described above is an appropriate method to describe the time-domain effects of the measurement of shock pressures on a rigid sphere.

In addition to removing the effects of the rigid sphere, the IRF can be used to predict the effects of a rigid sphere on an incident wave. For example, by convolving the reference pressure waveform shown in Fig. 6 with the IRF calculated to remove the effects of the probe, an estimate of the scattered field may be obtained. These predictions for the pressure on the surface of a rigid sphere at the three measurement angles are shown in Fig. 9. The convolutions show the expected delays in the shock arrival time. For example, the shock measured by the microphone at 57° is predicted to arrive a value of ct/a of 0.66 prior to the shock measured at 90° , while the value measured above is 0.50, and for the shock measured at 167° the predicted normalized time of arrival is 1.19, compared to the measured value of 1.21. Also, the shock strengths δ_L vary by 15%, 54%, and 0.6% relative to the incident shock for the predicted waveforms at 90° , 57° , and 161° on the surface of the sphere, respectively. The predicted waveforms therefore have greater phase changes and higher amplitudes than the measured waveforms. These errors may be due to the different measurement locations or the presence of wind in the measurement. However, notwithstanding these differences, the predicted shock fronts are sufficiently similar to those measured using the spherical probe to validate the use of an IRF derived from rigid-sphere scattering to assess the time-domain effects of shock measurements.

The above analyses show the validity of describing the measurement of shocks on a spherical probe with a linear scattering theory. Convolution of the IRF derived from rigid sphere scattering with a reference shock waveform is able to predict the effects of rigid sphere scattering on the shock strengths and arrival times to within 30% (and usually better

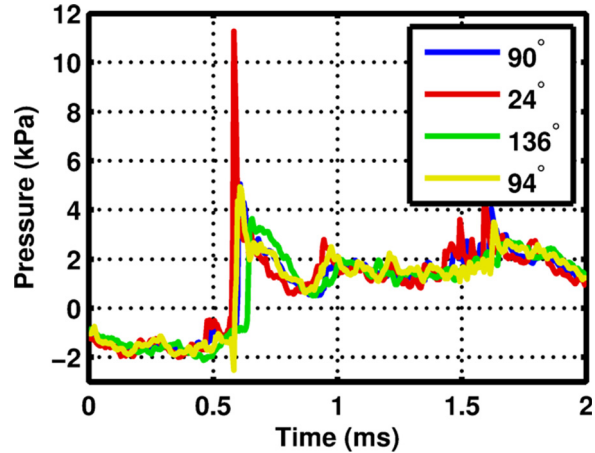


FIG. 10. (Color online) Portions of waveforms of noise radiating from a GEM-60 solid rocket motor measured by a spherical probe consisting of four microphones embedded in a rigid sphere.

than that) of the measured values despite some uncertainty in measurement angles. In addition, the numerical removal of the effects of the sphere allow estimates of the incident sound field, where the differences between the estimates from the different microphones are relatively small and allow for checks of self-consistency. These findings indicate that using the IRF on a rigid sphere would be an appropriate method to analyze the effect of shock measurements in the study of more complicated sources which may have more complicated waveforms containing shocks, such as noise radiating from solid rocket motors.

III. APPLICATION TO ROCKET NOISE

We now consider the application of this method to acoustical measurements that were taken during a static firing of a GEM-60 solid rocket motor, which is an 827 kN (186 000 lb) thrust motor designed to be used with a Delta IV orbital launch vehicle. Details of this test, which was conducted at the ATK T-6 test facility near Promontory, UT, were reported previously by Gee *et al.*¹ The spherical probe described above was placed 24 m downstream from the rocket nozzle exit and 9 m from the estimated shear layer edge. Portions of the waveforms measured by the four microphones embedded in the probe are shown in Fig. 10. The angles listed are the angles on the sphere assuming the sound field is locally planar and propagating in the direction of the maximum sound pressure level of far-field measurements (60° from the downstream direction). Since a rocket plume represents a distributed source whose extent and directionality varies with frequency and the surrounding terrain is nonuniform,¹ the plane wave-assumption may be poor. The direction of propagation was chosen based on near field-intensity estimates.^{1,19}

The delay in the arrival times and the variation in the peak shock amplitudes are similar to the predictions made for the balloon experiment described above, notwithstanding the fact that the simplified scattering model described in Sec. II does not fully apply to near-field rocket noise due to the complicated nature of the source and terrain. For example, consider the large shock near 0.6 ms in Fig. 10. The

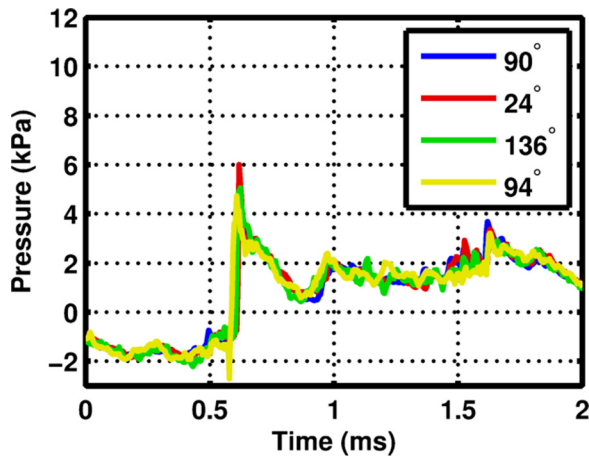


FIG. 11. (Color online) Estimates of the incident rocket noise waveform found by deconvolving the rigid-sphere impulse response function from the waveforms shown in Fig. 9.

microphones on the sphere surface at 90° , 24° , 136° , and 94° estimate a shock strength of 0.0712, 0.1362, 0.0460, and 0.0852, respectively, and arrive 0, -14.6 , 58.6, and $1.3 \mu\text{s}$ relative to the 90° microphone's arrival time, respectively. Similar to the above analysis, the microphone at the smallest angle predicts the largest shock strength, and the shock strengths decrease with increasing angle. Therefore, it is likely that deconvolving the impulse response function (IRF) for a rigid sphere from the rocket noise data will yield more accurate estimates of the true time-domain characteristics of the shock content in the rocket noise field at the location of the spherical probe.

The estimates of the incident waveform, found by deconvolving the IRF from the rocket noise data, are shown in Fig. 11. The estimates look qualitatively much more similar to each other than the original waveforms did. The estimates of the shock strength of the large shock around 0.6 ms become 0.0604, 0.0780, 0.0660, and 0.0679 for the microphones at 90° , 24° , 136° , and 94° , respectively, with time delays relative to the 90° microphone of 0, 19.5, 24.4, and $0 \mu\text{s}$, respectively. There are still some discrepancies between the waveforms in Fig. 11, especially away from shocks. For example, from 1 ms to 1.5 ms the general trend of all four waveforms is to start decreasing then slightly start increasing, but each waveform appears to have distinct, uncorrelated noise, varying by as much as 1 kPa from the other waveforms. It is interesting to note that similar uncorrelated noise has been observed in military aircraft noise.²⁰ This discrepancy and others like it may be due to the complexity of the environment and the source. Other factors that may cause these discrepancies are the nonlinearity (both cumulative and local) of the sound field, the response of the microphones used in the probe, and the electronics associated with the probe and data acquisition.

In addition to studying portions of the GEM-60 waveforms, studying aggregate quantities, such as spectra and statistical metrics, is also useful to visualize and quantify average behavior of time-domain phenomena for an entire waveform. First, the one-third octave band spectra are presented and discussed, followed by an analysis of the densities

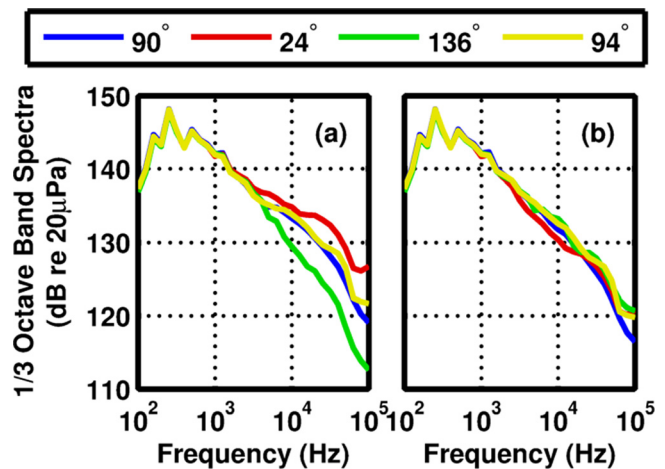


FIG. 12. (Color online) One-third octave band spectra of noise radiating from a static GEM-60 solid rocket motor firing (a) measured by a spherical probe and (b) the estimates of the incident field obtained by deconvolving the IRF from the waveforms measured on the surface of the probe.

of the pressure amplitudes and time-derivatives. The four one-third octave band spectra calculated from the spherical probe measured waveforms are presented in Fig. 12(a), and the spectra for the deconvolved estimates of the incident waveform based on the measured spectra are shown in Fig. 12(b). As expected from the frequency response function presented earlier, the main differences occur for high frequencies. The four spectra are nearly identical up to 1 kHz, and remain quite similar until about 4 kHz, after which they diverge significantly from each other, differing by about 15 dB at 100 kHz. As predicted by the frequency response analysis shown in Sec. II above, the microphone that measures the greatest levels for high frequencies is the microphone with the smallest angle relative to the assumed location of normal incidence ($\theta = 24^\circ$), and since none of the measurement locations is close to the back of the sphere, the high frequency levels tend to decrease for greater values of θ .

The spectra of the incident pressure wave estimates are much more similar to each other at high frequencies than the direct measurements, differing by less than 5 dB at 100 kHz. The spectra are not necessarily expected to be identical to each other, since the approximations necessary for this analysis may not be appropriate for this complicated system.

It is important to note that power spectra do not provide information on the time-domain statistics of a waveform. Another method of characterizing a waveform that does provide time-domain statistical information is the probability density function (PDF) of the pressure amplitudes. The PDFs of the pressure amplitudes of the waveforms measured by the spherical probe are shown in Fig. 13(a), and the distributions of incident-field estimates are shown in Fig. 13(b). As can be seen in Fig. 13(a), there is not much variation between the PDFs measured at different angles below 5 kPa. Above 5 kPa, the PDFs become slightly more varied—differing by up to a factor of 3 from each other—with the most dramatic difference being the higher probability of very high amplitudes for the $\theta = 24^\circ$ microphone, due to the pressure increase associated with reflections. These slight differences are nearly gone

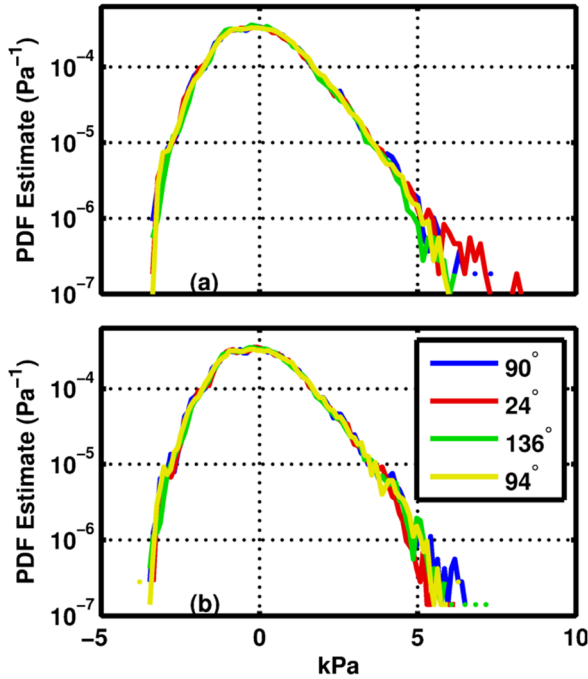


FIG. 13. (Color online) Estimates of the probability density function of the pressure amplitudes of noise radiating from a GEM-60 solid rocket motor, (a) measured by a spherical probe and (b) the same for the estimates of the noise field incident upon the sphere.

in Fig. 13(b), indicating that the high-amplitude differences are, indeed, due to the presence of the rigid sphere.

As shown by Muhlestein *et al.*,²¹ the pressure amplitude PDF does not vary significantly for nonlinearly propagating waves. The PDF of the time-derivatives of the pressure amplitudes is much more sensitive to the evolution of high-amplitude waveforms due to the growth and evolution of shocks. The PDFs of the time-derivative of the pressure amplitudes of the waveforms measured by the spherical probe are shown in Fig. 14(a), and the PDFs of incident-field estimates are shown in Fig. 14(b). The values of the time-derivatives studied for this paper were estimated using a finite-difference scheme. There are dramatic differences between the tails of the four measured PDFs shown in Fig. 14(a), with variations of more than an order of magnitude. Recalling that the presence of the sphere tends to increase shock strength for small angles and decrease shock strength for angles in the shadow region of the sphere, it makes sense that the measurement with the largest probability of very large time-derivatives is the $\theta = 24^\circ$ measurement, and the measurement with the lowest probability of large time-derivatives is the $\theta = 136^\circ$ measurement. Also, notice the PDFs of the time-derivative of the incident-field pressure estimates shown in Fig. 14(b) are very similar to each other, further indicating that the variations in Fig. 14(a) are likely due to the presence of the rigid spherical probe.

In order to quantitatively compare PDFs, various statistical measures have been defined. The mean and variance are well known. For example, acoustic processes are by definition zero-mean processes, and the variance of a zero-mean process is the mean-square of the process, which is used in the definition of the overall sound pressure level. The

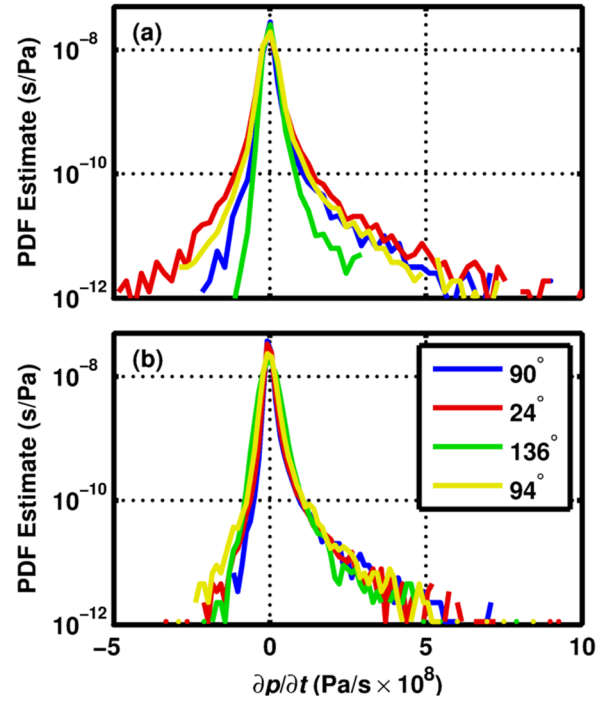


FIG. 14. (Color online) Estimates of the probability density function of the time-derivative of the pressure amplitudes of noise radiating from a GEM-60 solid rocket motor, (a) measured by a spherical probe and (b) the same for the estimates of the noise field incident upon the sphere.

skewness of a PDF ($Sk\{x\}$ for a PDF of the variable x) is a normalized measure of the asymmetry of the PDF. If a PDF has a long tail on the positive side of the PDF (for example, the PDFs of the time-derivative of pressure amplitudes), then the PDF has a positive skewness, and if the tail is on the negative side of the PDF, then the PDF has a negative skewness. Ffowcs Williams identified the skewness of the pressure as an indicator of “crackle” in high-velocity jet noise.²² However, Gee *et al.* have shown that “crackle” is more likely due to the presence of shocks generated by finite-amplitude effects.^{23,24} Since shocks have rapid pressure rises, the skewness of the time-derivative of the pressure has also been identified as a way to quantify the effects of nonlinearity on jet noise.^{25,26} The variance of the pressure amplitude and time-derivative of pressure amplitude PDFs, both with and without the effects of the spherical probe, are given in Table III and the skewness of the pressure amplitude and time-derivative of pressure amplitude PDFs, both with and

TABLE III. Summary of the variance values for the distributions of the pressure amplitude and of the time-derivative of the pressure amplitudes. The subscript *inc* indicates the incident field estimate obtained from the variable.

θ	90°	24°	136°	94°
$\text{Var}\{p(\theta, t)\}(\text{kPa})^2$	1.62	1.66	1.52	1.61
$\text{Var}\{p(\theta, t)_{inc}\}(\text{kPa})^2$	1.62	1.55	1.55	1.61
$\text{Var}\left\{\frac{\partial p(\theta, t)}{\partial t}\right\}\left(\frac{\text{Pa}}{\text{s}} \times 10^7\right)^2$	8.53	22.3	3.09	1.15
$\text{Var}\left\{\frac{\partial p(\theta, t)}{\partial t}\right\}_{inc}\left(\frac{\text{Pa}}{\text{s}} \times 10^7\right)^2$	5.44	6.48	8.27	8.09

TABLE IV. Summary of the skewness values for the distributions of the pressure amplitude and of the time-derivative of the pressure amplitudes. The subscript *inc* indicates the incident field estimate obtained from the variable.

θ	90°	24°	136°	94°
$\text{Sk}\{p(\theta, t)\}$	0.510	0.617	0.505	0.474
$\text{Sk}\{p(\theta, t)_{inc}\}$	0.495	0.451	0.530	0.473
$\text{Sk}\left\{\frac{\partial p(\theta, t)}{\partial t}\right\}$	11.5	9.42	3.70	5.99
$\text{Sk}\left\{\frac{\partial p(\theta, t)}{\partial t}\Big _{inc}\right\}$	11.6	10.3	3.36	5.99

without the effects of the spherical probe, are given in Table IV. The statistical measures are much more similar for the incident field estimates, especially the variance of the estimates of the incident time-derivative of pressure. This similarity suggests that the impulse response function for a plane wave on a sphere developed in Sec. II is an appropriate way to model the effects of the rigid spherical intensity probe on these pressure measurements of a rocket noise field.

IV. CONCLUSIONS

A method to describe the pressure measured on the surface of a rigid sphere due to an incident arbitrary linear planar waveform has been developed using Fourier techniques. This method is encapsulated in the measurement-angle dependent impulse response function (IRF) on the surface of a rigid sphere. This method of describing diffraction was validated by comparing blast noise from an exploding balloon measured by an array of microphones embedded in a rigid sphere with the measurement of a reference microphone. The IRF performs well, but it requires a large number of frequencies to resolve transient signals. The application of the IRF to propagating shock waves can help guide the intuition of those studying the diffraction of shock waves around instrumentation by showing the effect of shock reflection from curved surfaces and of shadow zones on the measurement of peak pressure values and rise times associated with shocks. The IRF on the surface of a rigid sphere was applied to rocket noise measurements in order to describe diffraction around a spherical intensity probe. The estimations of the incident wave were very similar to each other in terms of the shape of the waveforms, location of shocks, and the pressure and time-derivative of pressure statistics in addition to intensity estimates.

The accuracy and ease of numerical implementation of this relatively simple model suggests that other Fourier-based approaches to the scattering of shocks from objects may be similarly beneficial in reducing the effect of measurement equipment on data and improving the quality of measurements. Using boundary-element and finite-element modeling, the pressure due to incident shock waves on the surface of objects more complicated than a rigid sphere may be estimated.

- ¹K. L. Gee, J. H. Giraud, J. D. Blotter, and S. D. Sommerfeldt, "Energy-based acoustical measurements of rocket noise," in *15th AIAA/CEAS Aeroacoustics Conference*, Miami, FL (May 11–13, 2009).
- ²Brüel & Kjaer, *Microphone Handbook* (Nærum, Denmark), Chap. 2, pp. 45–48 (1996).
- ³T. B. Gabrielson, T. M. Marston, and A. A. Atchley, "Nonlinear propagation modeling: Guidelines for supporting measurements," in *Proc. Noise-Con*, 2005, Minneapolis, pp. 275–282.
- ⁴G. W. Elko, "An acoustic vector-field probe with calculable obstacle bias," *NOISE-CON* **91**, 525–532 (1991).
- ⁵A. Sommerfeld, "The theoretical X-ray diffraction" ("Theoretisches über die Beugung der Röntgenstrahlen"), *Z. Math. Phys.* **46**(11), 1901.
- ⁶H. Lamb, "On the diffraction of a solitary wave," *Proc. London Math. Soc.* **2**(8), 422–437 (1910).
- ⁷K. M. Mitzner, "Numerical solution for transient scattering from a hard surface of arbitrary shape-retarded potential technique," *J. Acoust. Soc. Am.* **42**(2), 391–397 (1967).
- ⁸H. Tanno, K. Itoh, T. Saito, A. Abe, and K. Takayama, "Interaction of a shock with a sphere suspended in a vertical shock tube," *Shock Waves* **13**, 191–200 (2003).
- ⁹C. Feuillade, "Animations for visualizing and teaching acoustic impulse scattering from spheres," *J. Acoust. Soc. Am.* **115**(5), 1893–1904 (2004).
- ¹⁰K. L. Gee, J. H. Giraud, J. D. Blotter, and S. D. Sommerfeldt, "Near-field vector intensity measurements of a small solid rocket motor," *J. Acoust. Soc. Am.* **128**(2), EL69–EL74 (2010).
- ¹¹D. T. Blackstock, M. F. Hamilton, and A. D. Pierce, "Progressive waves in lossless and lossy fluids," in *Nonlinear Acoustics* (Acoustical Society of America, New York, 2008), pp. 65–150.
- ¹²V. W. Sparrow and R. Raspet, "A numerical method for general finite amplitude wave propagation in two dimensions and its application to spark pulses," *J. Acoust. Soc. Am.* **90**(5), 2683–2691 (1991).
- ¹³R. Raspet, J. Ezell, and S. V. Coggeshall, "Diffraction of an explosive transient," *J. Acoust. Soc. Am.* **79**(5), 1326–1334 (1986).
- ¹⁴N. A. Logan, "Survey of some early studies of the scattering of plane waves by a sphere," *Proc. IEEE* **53**(8), 773–785 (1965).
- ¹⁵P. M. Morse and K. U. Ingard, *Theoretical Acoustics* (Princeton University Press, Princeton, NJ, 1968), pp. 418–441.
- ¹⁶A. D. Pierce, *Acoustics* (Acoustical Society of America, Woodbury, NY, 1989), pp. 425–431.
- ¹⁷M. B. Muhlestein, K. L. Gee, and J. H. Macedone, "Educational demonstration of a spherically propagating acoustic shock," *J. Acoust. Soc. Am.* **131**(3), 2422–2430 (2012).
- ¹⁸S. Temkin, "Attenuation of guided, weak sawtooth waves," *J. Acoust. Soc. Am.* **46**, 267–271 (1969).
- ¹⁹M. James and K. L. Gee, "Advanced acoustic measurement system for rocket noise source characterization," in *Internoise 2012*, New York (2013), pp. 7602–7614.
- ²⁰T. B. Neilsen, K. L. Gee, A. T. Wall, and M. M. James, "Similarity spectra analysis of high-performance jet aircraft noise," *J. Acoust. Soc. Am.* **133**(4), 2116–2125 (2013).
- ²¹M. B. Muhlestein and K. L. Gee, "Experimental investigation of a characteristic shock formation distance in finite-amplitude noise propagation," *POMA* **12**, 045002 (2014).
- ²²J. E. Ffowcs-Williams, J. Simson and V. J. Virchis, "'Crackle': An annoying component of jet noise," *J. Fluid Mech.* **71**(2), 251–271 (1975).
- ²³K. L. Gee, V. W. Sparrow, M. M. James, J. M. Downing, C. M. Hobbs, T. B. Gabrielson, and A. A. Atchley, "Measurement and prediction of noise propagation from a high-power jet aircraft," *AIAA J.* **45**(12), 3003–3006 (2007).
- ²⁴K. L. Gee, T. B. Neilsen, M. B. Muhlestein, A. T. Wall, J. M. Downing, and M. M. James, "On the evolution of crackle in jet noise from high-performance engines," *AIAA Pap.* 2013–2190 (2013).
- ²⁵S. A. McNerny, "Launch vehicle acoustics Part 2: Statistics of the time domain data," *J. Aircraft* **33**(3), 518–523 (1996).
- ²⁶S. A. McNerny and S. M. Ölçmen, "High-intensity rocket noise: Nonlinear propagation, atmospheric absorption, and characterization," *J. Acoust. Soc. Am.* **117**(2), 578–591 (2005).